2026 IEEE International Conference on Robotics and Automation (ICRA 2026)
June 1-5, 2026. Vienna, Austria

SeaViper: An Efficient Thin 2D Surface-Swimming Soft Robot

Elias Veilleux, Hsin Cheng, Zhiwu Zheng
Sigurd Wagner, Naveen Verma, James C. Sturm and Minjie Chen
Princeton University, Princeton NJ, 08544

***Abstract*— This paper introduces SeaViper, a *soft extendable aquatic vibrating intelligent piezoelectric robot* that extends previously developed land-based systems into the aquatic domain. The aquatic domain introduces new fundamental mechanisms of motion as well as new robot-platform requirements. To study these, we present the mechanical and electrical design of SeaViper and investigate the drive–frequency response of three prototype configurations, with energy efficiency as a key design consideration. The prototypes achieve a peak velocity of up to 33.2 cm/s (1.38 body-length per second) with an estimated power of 2 W and a minimum cost of transport (CoT) of 3.9, significantly improving upon the performance of the prior land prototype. Measured thrust data combined with current-sense analysis enable estimation of useful mechanical output and end-to-end electromechanical efficiency. Velocity and CoT are benchmarked against both other robotic swimmers and aquatic animals, highlighting the general gap to biological performance. To further advance the sheet-like, untethered design, the aquatic prototype integrates a microcontroller, wireless communication, sensing, and on-board battery charging circuitry, paving the way for future bio-inspired morphologies at the air–water interface with advanced driving patterns.**

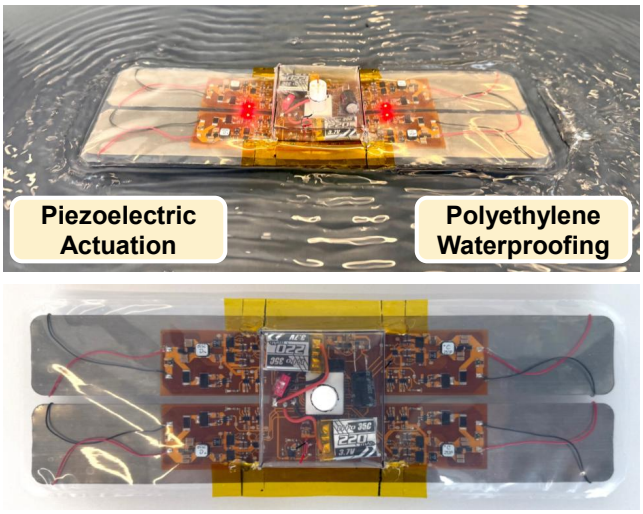

Fig. 1. SeaViper prototype in motion. Small gaps in the steel sheet create the four-legged "H" frame. Each leg is driven via 300 V piezoelectric actuators. The design is insulated from water using polyethylene sheets.

I. Introduction

The field of soft robotics is a rapidly developing space characterized by the use of compliant materials, bio-inspired designs, and structures with effectively continuous degrees of freedom [1]. These properties enable collision resilience, safe human interaction, and complex, adaptive motion—features that remain challenging for traditional rigid robots [2]. Within this field, aquatic soft robotics has drawn increasing interest for applications in environmental monitoring, marine biology, and search-and-rescue [3]–[5]. Designs span orders of magnitude in length scale, from millimeter-scale swimmers [6] to those approaching a meter in length [7], making direct performance comparisons challenging. Metrics such as body-normalized velocity and cost of transport (CoT) have therefore become standard tools for cross-scale evaluation [8], [9].

Here, we develop a surface-swimming prototype based on our previously developed eViper topology [10]–[12], a modular and scalable piezoelectric-actuated system. This prototype is referred to as "SeaViper", a ***S**oft **E**xtensible **A**quatic **V**ibrating **I**ntelligent **P**iezo**E**lectric **R**obot*. The design incorporates the 4-actuator, 2D "H"-frame of the ground prototype reported in [11], while incorporating a waterproof polyethylene exterior, onboard battery charging, integration of the ESP32 microcontroller, and a compacted PCB layout. The water prototype achieves a notably higher speed of 33.2 cm/s with an estimated power consumption of about 2 W compared with 3.6 cm/s at roughly 1 W for the ground prototype in [11].

The aquatic environment is well suited for future exploration of this robotics platform, and introduces fundamentally different physics and design constraints compared to a ground platform. Whereas a land prototype generates thrust by point-contact frictional forces, the aquatic prototype moves via momentum exchange and the generation of capillary-gravity waves in the water. Buoyancy and hydrodynamic drag become important design considerations, and hydrodynamic loading shifts the structural resonant frequency and motivates careful consideration of actuator geometry and operation frequency.

In this work, we present the first surface-swimming implementation of the SeaViper platform, perform a comparative analysis of three actuator-substrate pairings, and provide an end-to-end analysis of electrical-to-mechanical energy efficiency. In doing so, we offer insights into methods of improving the CoT in future work. The modular, scalable, and planar nature of the design allows it to serve as a foundation for future bio-inspired variants, such as eel- or stingray-inspired morphologies, enabling further exploration of soft robotic locomotion at the air-water interface.

979-8-3315-8160-2/26/$31.00 ©2026 IEEE

TABLE I

PROTOTYPE DIMENSIONS AND MASS

Prototype	Steel Sheet	Actuator	Mass
SW (Short Wide)	7.0 × 20.0	6.7 × 3.1	50.8
LN (Long Narrow)	7.5 × 26.5	10.0 × 1.8	54.2
LW (Long Wide)	7.5 × 26.5	10.0 × 3.1	63.4

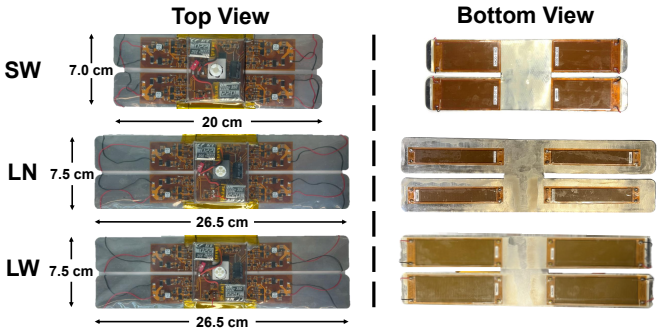

Fig. 2. Three prototypes were designed, using different geometries and piezoelectric actuators. These differences lead to distinguishable resonant frequencies between models, as detailed in section IV-B.

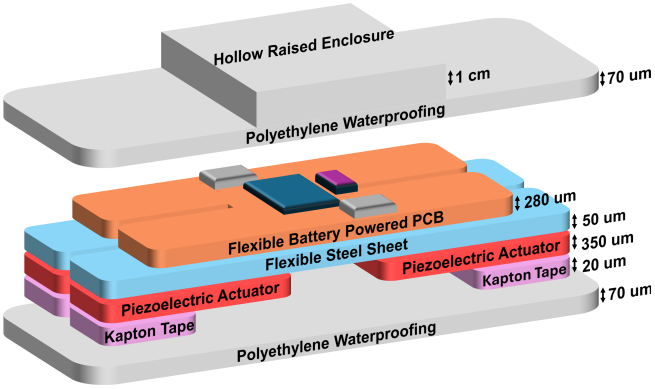

Fig. 3. SeaViper's structural layering. The steel-sheet and piezoelectric actuator are glued together, with the flexible PCB placed on top. These layers are surrounded by heat-sealed polyethylene layers for waterproofing. The bottom polyethylene layer is adhered to the steel-sheet and actuators to guarantee a uniform surface in contact with the water, measuring less than 1 mm thick in total. The top waterproofing layer is loosely adhered, creating a region of trapped air for buoyancy, as described in Sect. II-A. The central enclosure is notably taller than the rest of the structure, at approximately 1 cm.

II. HARDWARE IMPLEMENTATION

A. Mechanical Platform

The SeaViper platform adopts the general two-dimensional "H"-frame architecture of [11]'s ground-based platform but is adapted for operation at the air–water interface. An ESP32 microcontroller is placed at the center of the design, with batteries positioned on either side for balance, as seen in Fig. 1 and Fig. 3. Each of the four legs is driven by a 300 V type-2 Macro Fiber Composite (MFC) actuator from Smart Material Corporation [13] bonded to a flexible steel substrate. All designs follow a thin multi-layer structure: a 350 µm piezoelectric actuator adhered to the underside of a 50 µm flexible steel sheet, topped by a customized 4-layer flexible PCB. Three actuator–substrate configurations were fabricated, with dimensions described in Table I and Fig. 2. These prototypes were selected to investigate the effects of actuator width, length, and overall system mass on performance. Their labeling describes the actuator dimensions of the prototype – SW: Short Wide, LN: Long Narrow, LW: Long Wide.

Waterproofing the topology was a critical design consideration, guided by three constraints: (1) the structure must remain flexible, (2) mass contribution should be minimal while trapping air for buoyancy, and (3) sealing must be robust. Modeling the prototypes as rectangular prisms according to the steel sheet dimensions (Table I), one would expect the SW, LN, and LW designs to rest 3.6, 2.7, and 3.2 mm below the water surface respectively. In practice, the resting level is not quite this deep, due to the capillary force not accounted for in this model. Given the sub-millimeter thickness of the prototype itself, this requires the top waterproof layer be loosely adhered such that a few millimeters of air are trapped in the design. To achieve this, the final solution employed two heat-sealed polyethylene sheets: a flat lower layer and a folded upper layer forming a raised boxlike central enclosure around the microcontroller and batteries due to their height. Seams in the upper enclosure were sealed with hot glue. This design preserved flexibility, minimized weight, and provided a waterproof air cavity (Fig. 1).

B. Electrical Platform

Two 220 mAh, 3.7 V lithium-polymer batteries connected in series provide 7.4 V nominal (charged to 8.2 V peak) to the robot. A 2.2 mF electrolytic capacitor is placed across the supply to help stabilize the voltage rail. The robot can perform standard operations for approximately 40 minutes before batteries are recharged.

To drive the piezoelectric actuators, the 7.4 V battery supply is stepped up to 300 V dc using a modified version of [12]'s reported power-conversion topology. The first stage is an LLC resonant converter: the dc input is inverted by a full-bridge inverter to produce an ac waveform, which is then filtered to suppress switching harmonics. This signal is stepped up a factor of twenty by a transformer. A single-stage Cockcroft–Walton (CW) voltage multiplier doubles and rectifies the voltage to the final 300 V, after which a discharge circuit regulates the actuator load voltage. Additional CW stages can be cascaded to operate piezoelectric actuators at higher voltages. The aquatic prototype utilizes only 300 V P2 actuators, so only a single CW stage was implemented to minimize mass and PCB footprint. The smaller PCB area enabled the study of the reduced steel sheet size used in the SW prototype.

The converter stages fit within the area of the steel legs, forming a modular building block out of the actuator, steel sheet, and power converter which can be replicated in other two-dimensional designs. The ESP32 microcontroller has been integrated directly into the flexible PCB, eliminating

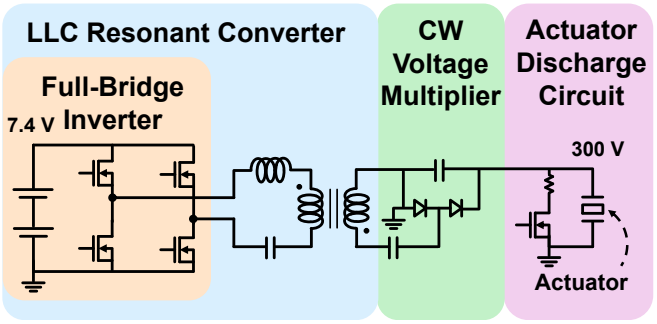

Fig. 4. Block diagram of the power converter module. The output voltage can be configured by chaining multiple Cockcroft-Walton stages together. SeaViper prototypes use only a single stage of the CW voltage multiplier, thus reducing PCB area. MOSFET gate signals are controlled by the integrated microcontroller.

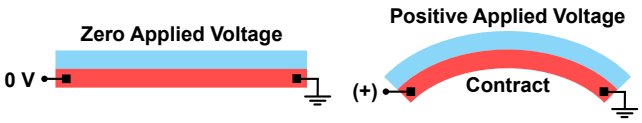

Fig. 5. When positive voltage is applied, contraction in the piezoelectric actuator induces concave-down bending in the actuator-substrate pair. Maximum allowable bending is achieved at approximately 300 V.

the need for a separate rigid development board and reducing both mass and profile height. This integration also enhances the compliance of the overall structure.

Since the sealed waterproof housing prevents battery removal, an LTC4079 charging IC was integrated to enable in-situ recharging. Short leads pass through the waterproof layer to connect to an external supply during charging.

III. Experimental Methods

A. Operating Principle of the Prototype

Motion in the SeaViper arises from the coupled piezoelectric actuator and steel sheet substrate. When a 300 V potential is applied, the piezoelectric layer contracts, producing a concave-down bending of the composite sheet, as shown in Fig. 5. Removal of the potential returns the structure toward its equilibrium state. Unlike a ground robot built with this topology, which interacts with the environment at discrete foot contact points, the bottom surface of the aquatic prototype maintains continuous contact with the air–water interface. This continuous contact eliminates slip and random jitter from foot placement and allows each cycle to produce a more repeatable thrust impulse. Each actuation cycle generates capillary–gravity waves and imparts momentum into the surrounding fluid, resulting in opposing momentum transfer to the robot. Because the surrounding water adds inertia and damping (see Sec. IV-B), the robot's response depends on both its own structure and the local fluid mass. This mechanism enables both translational and rotational motion.

Control of the robot is achieved by modulating the actuation signals applied to the four legs. The primary degrees of freedom in the drive signals are frequency, phase relationships between actuators, and duty ratio. To reduce this parameter space, we focus on two canonical driving modes:

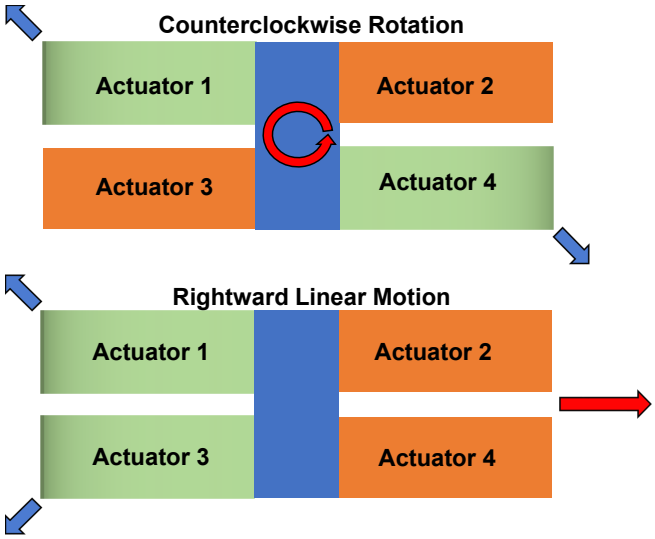

Fig. 6. The two primary driving modes of SeaViper. Actuators of the same color are paired and have identical driving parameters. In this work, SeaViper is primarily operated with one pair active and one pair idle ($D = 0\%$). In this illustration, green indicates the active pair while orange indicates the idle pair. Blue arrows indicate the general direction of momentum imparted into the water by a given actuator, while the red arrow signifies the general net force or torque experienced by the prototype.

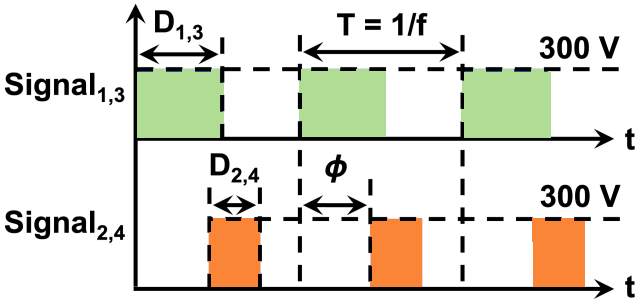

Fig. 7. Example linear mode waveforms demonstrating the configurable parameters in the 300 V square pulse sent to the actuators. D, the duty ratio, indicates the percent on time over a period. ϕ is the relative phase of the pulse, and T is the period of the waveform.

1. **Rotational mode:** diagonal actuator pairs (green and orange, respectively) are driven in phase with identical duty ratio and frequency, producing a net torque about the robot's center of mass.

2. **Linear mode:** adjacent actuator pairs (green and orange, respectively) are driven in phase with identical duty ratio and frequency, producing a net forward thrust.

These actuation principles are illustrated in Fig. 6 and Fig. 7. For most experiments, only two actuators were driven simultaneously. Driving both actuator pairs concurrently was found to generate partially opposing forces that reduced translational and rotational velocities. A notable exception was observed near structural resonance, where the LN prototype achieved significantly higher velocity of 32.2 cm/s when all actuators were driven simultaneously (Fig. 10 B). This shows that coordinated four-leg actuation at resonance can improve performance. However, this motion is currently too

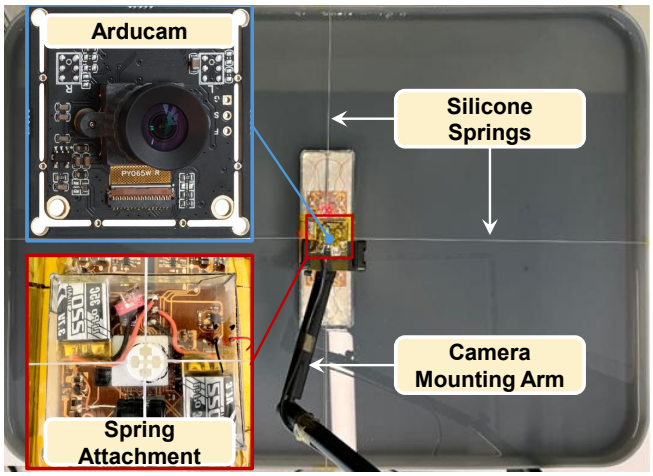

Fig. 8. Data collection environment, depicted for the thrust measurement application. Note the thin silicone springs in each cardinal direction. The pool is filled 4 cm deep, with a camera placed above to observe displacement of the prototype. Springs attach to the center of the prototype via a central column. When observing dynamic performance, the springs were removed and the robot was allowed to traverse from end-to-end.

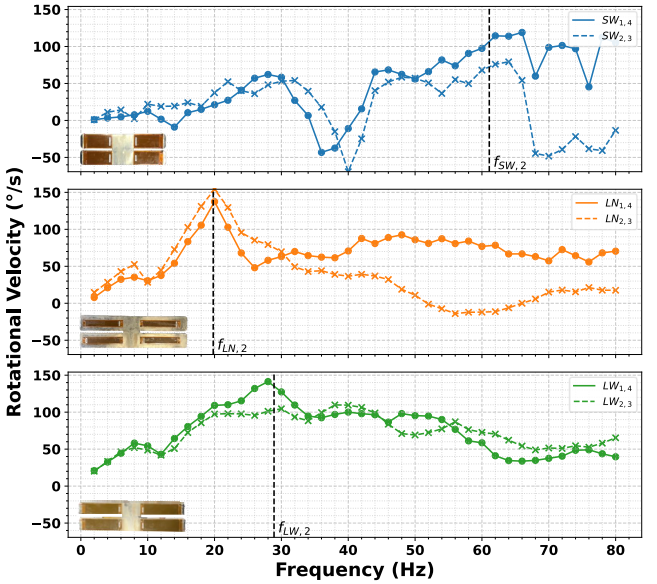

Fig. 9. Observed rotational velocity generated when sweeping the operating frequency of SeaViper at $D_{1,4} = 50\%$, $\phi = 0$. Notable peaks emerge corresponding to the theoretical second bending modes of the three SeaVipers. The dashed line corresponds to counterclockwise rotation using actuators 1 and 4, while the solid line corresponds to clockwise rotation using actuators 2 and 3.

extreme for the prototypes, causing their front to submerge shortly after reaching this top speed. For this reason, data collection focused on two-actuator driving modes.

B. Testing Environment

Two testing environments were used for the study of the prototype. The velocity and thrust data were collected in a small shallow $100\times70\times6$ cm^3 pool. Performance was then validated in a deeper, larger environment ($254\times134\times40$ cm^3) to verify that reflections, edge effects, and ground effects were not significant contributions. This larger pool was also used for demonstration of path-tracking control of the prototype, discussed in Section IV-E.

Translational and rotational velocity were measured via a 100 Hz ArduCam UC844 camera tracking an ArUco marker at the center of the prototype as it traversed the pool, and later analyzed using OpenCV. A calibrated spring-based platform was developed for preliminary measurement of static thrust. In this design, springs are attached as shown in Fig. 8, and thrust measurements are extracted from the displacement and rotation of the new equilibrium position the robot arrives at during actuation.

IV. Experimental Results

A. Data Analysis of Basic Robot Motion

To characterize the rotational frequency response, each prototype was driven in rotational mode with $D = 50\%, \phi = 0\%$, and the drive frequency swept from 2 to 80 Hz in 2 Hz increments (Fig. 9). Steady-state angular velocity was extracted from this trajectory. Notable peaks appear in the rotational data, consistent with the legs' theoretical second bending modes (see Sec. IV-B).

Across designs (Fig. 9), the LN prototype exhibits the lowest rotational resonance at 20 Hz, followed by LW at 28 Hz. The SW prototype shows a less smooth response, with a peak near 64 Hz but direction reversals between 32-42 Hz and at frequencies above resonance. The fastest rotational performance occurs with the LN performance at 154.2 °/s, closely followed by the LW prototype at 141 °/s.

Assessing the linear frequency response required a small modification to the linear mode. In typical linear operation, the actuator and structural asymmetries introduce a systematic yaw, reducing the measured forward speed. To isolate the achievable forward velocity with respect to frequency, a compensatory phase bias ($|\Delta\phi| \leq 20\%$) was applied to one actuator of the active pair. The sign of $\Delta\phi$ sets the yaw direction. By alternating the sign of this phase bias, the linear orientation was maintained, allowing for full acceleration. The resulting data shown in Fig. 10 thus illustrates the maximum usable forward speed that one might attain during path-tracking and autonomous operation. With $|\Delta\phi| \leq 20\%$, the SW prototype was unable to attain linear motion between 22-26 Hz using actuators 2 and 4. For that reason, those points are excluded from the data.

Again, peak performance for each prototype occurs in the vicinity of their second bending modes. This behavior is characterized by a steep ascent in velocity as frequency increases toward resonance, while a slower decay in velocity as frequency increases beyond. This can be explained by the fact that the average thrust is generally a product of frequency of stroke, and impulse per stroke. Though impulse per stroke decreases past resonance, the increase in frequency slows the descent in attained velocity. In testing, the LW prototype was able to attain a significant 33.2 cm/s (1.37 BL/s) velocity at 28 Hz. However, minimum CoT is attained with the LN model traveling 27.3 cm/s at 20 Hz. Using power consumption data obtained via a current sense amplifier on

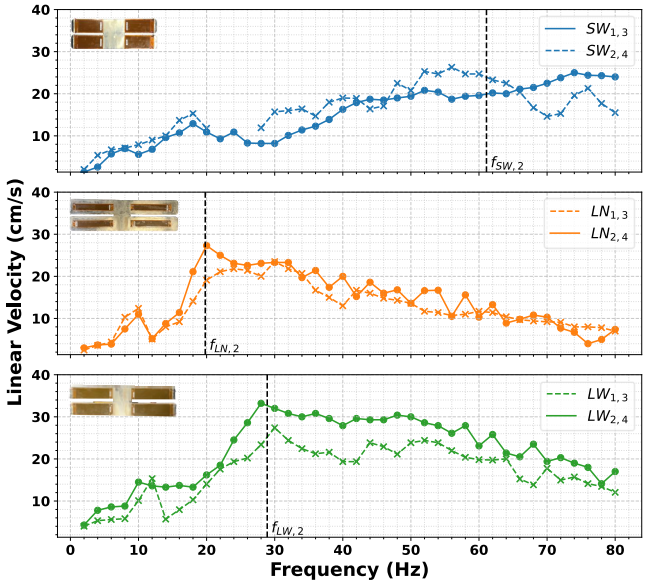

Fig. 10. Observed linear velocity generated when sweeping the operating frequency of SeaViper at $D_{1,3} = 50\%$, with $|\Delta\phi| \leq 20\%$ steering correction as described in IV-A. Peak velocities occur near the theoretical second bending modes of the prototypes. The dashed line corresponds to rightward linear motion using actuators 1 and 3, while the solid line corresponds to leftward motion using actuators 2 and 4. $SW_{1,3}$ data is absent from 22-26 Hz for reasons explained in Sect. IV-A

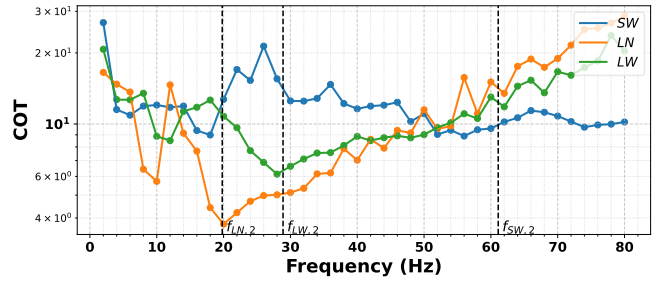

Fig. 11. Cost of transport vs frequency for the three prototypes, plotted using peak achieved linear velocity and current sense amplifier data to measure input power. All prototypes achieve optimal CoT near their theoretical second resonant mode, with the LN model reaching the lowest CoT of 3.9 at 20 Hz. This data-point is further discussed in section IV-C.

the robot, the CoT is plotted for each prototype against frequency in Fig. 11.

B. Theoretical Resonance Modeling of Cantilever Legs

An approximate theoretical model of the leg resonance frequencies was developed using fundamental cantilever beam analysis [14] [15]. The actuator, steel sheet, and bottom polyethylene layer are treated as a homogenized three-layer composite, with the actuators assumed to cover the entire length of the steel sheet for simplicity. Resonance frequencies were first calculated in air, followed by a fluid–structure interaction correction to estimate frequencies at the air-water interface.

The ith resonance frequency of a fixed-free cantilever in

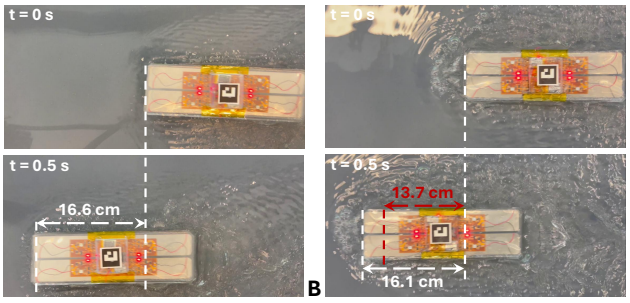

Fig. 12. A: Half a second of record observed leftward motion in Fig. 10, corresponding to the LW prototype driving actuator 2 and 4 at $f = 28$ Hz, $D = 50\%$, and $|\Delta\phi| = 10\%$ alternated as described in Sect. IV-A. B: Resonant four-actuator performance of the LN prototype over half a second moving leftward ($D = 50\%, \phi = 0$), contrasted with the record LN two-actuator performance in red. This operation consumes notably more power and thus remains less efficient than 2 actuator operation, despite being faster.

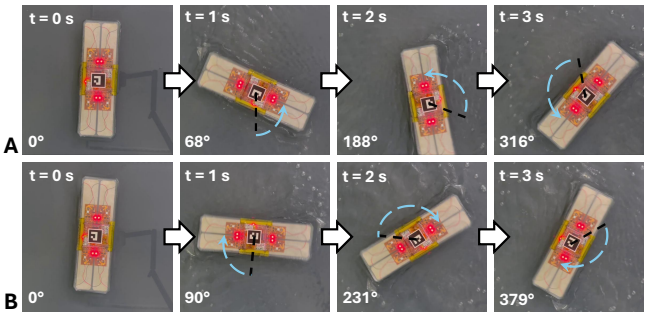

Fig. 13. A: Fastest counterclockwise rotation of the LN prototype, for actuators 2 and 3 operating in the rotational mode starting from rest: $f = 20$ Hz, $D = 50\%, \phi = 0$. B: Fastest clockwise rotation of the LN prototype, for actuators 1 and 4 operating in the rotational mode starting from rest: $f = 20$ Hz, $D = 50\%, \phi = 0$. Clockwise rotation is quite stable about the center of mass, while counterclockwise rotation occurs with a slight drift of the center of mass. Counterclockwise rotation reaches maximum angular velocity (137.4 °/s) after approximately 6 s, while clockwise reaches maximum angular velocity (154.2 °/s) after approximately 5 s.

air is given by

$$f_{a,i} = \frac{1}{2\pi}\frac{\lambda_i^2}{L^2}\sqrt{\frac{EI_b}{\rho_b A_b}}, \tag{1}$$

where λ_i are the eigenvalues of the Euler–Bernoulli beam equation, L is the leg length, EI_b is the flexural rigidity of the beam, ρ_b is the density of the beam, and A_b its cross-sectional area. Using this formula, the first three natural frequencies in air were calculated as: LN = [11.6, 73.0, 204.3] Hz, LW = [13.8, 86.5, 242.3] Hz, and SW = [26.7, 167.6, 469.3] Hz.

To account for hydrodynamic loading, an added-mass correction was applied:

$$\frac{f_{w,i}}{f_{a,i}} = \left[1 + \alpha\,\frac{\pi\rho_w W}{4\rho_b H_b}\,\Gamma_f(k_i)\right]^{-\frac{1}{2}}, \tag{2}$$

where $f_{w,i}$ is the resonant frequency at the air–water interface, ρ_w is the density of water, W the beam width, H_b the beam thickness, k_i the mode index, and $\Gamma_f(k_i)$ the hydrodynamic function. The scalar factor α accounts for reduced fluid coupling at the free surface compared to

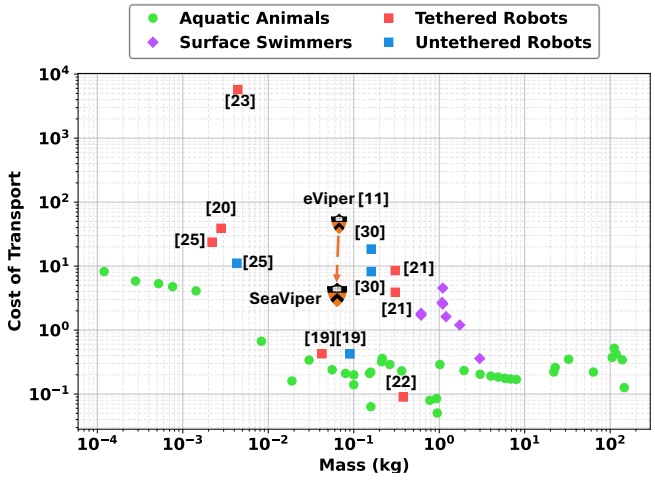

Fig. 14. The cost of transport of various animals and bio-inspired soft robotics systems. Animal data were acquired from [9], [18]. The small crest indicates the ground prototype performance from [11], while the larger indicates the best performance of the aquatic prototype.

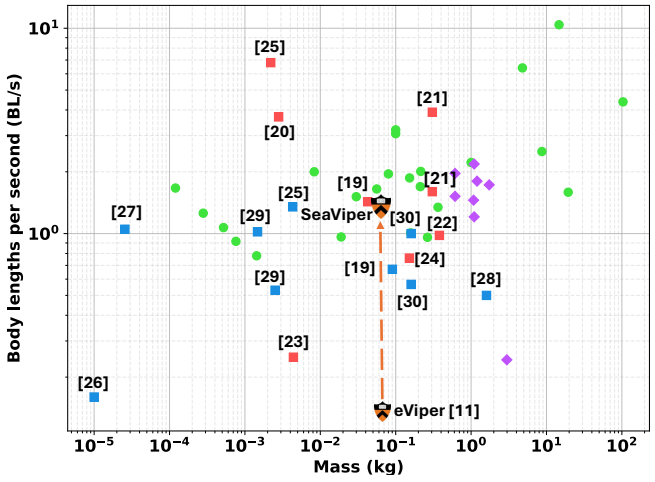

Fig. 15. The relative velocity of various animals and tethered and untethered aquatic soft robots. Untethered robots tend to under-perform tethered robots in this metric due to the additional mass of integrated power electronics and control. SeaViper improves upon the ground prototype's velocity by an order of magnitude, pushing it to the forefront of untethered soft aquatic submerged robot speeds. The small crest indicates the ground prototype performance from [11], while the larger indicates the best performance of our aquatic prototype. Figure developed from [8].

full submersion. Experimental studies on partially submerged cantilever beams confirm that added mass is significantly lower than in full immersion ($\alpha = 1$) [16], and potential-flow analyses show that for simple geometries such as spheres the added mass equals half the displaced fluid mass [17]. Guided by these precedents, we adopt $\alpha = 0.5$. This yields aquatic resonance frequencies of LN = [2.9, 19.8, 61.1] Hz, LW = [4.3, 28.9, 88.5] Hz, and SW = [9.0, 61.1, 187.0] Hz.

The theoretical second-mode resonances correspond closely to the observed behavior of the LN and LW prototypes in Figs. 9 and 10, validating the usefulness of the simplified model. Discrepancy between the theoretical model and experimental results are believed to arise from variation in layer thickness, effective stiffness, and bonding quality between the piezoelectric actuator and the steel substrate. As predicted by the model, the greater flexural rigidity of the LW prototype shifted its resonant frequency higher than the LN prototype. Similarly, the SW prototype exhibits an upward shift in optimal frequency relative to the longer LW prototype. However, the SW prototype shows less quantitative agreement with the model, suggesting that geometric effects or non-uniform bonding alter its effective hydrodynamic loading. These discrepancies motivate future finite-element modeling of the coupled fluid–structure system to capture effects beyond the scope of the present hydrodynamic-correction-based approach.

C. Performance Comparison and Cost of Transport Analysis

Cost of transport (CoT) is a widely used metric for comparing locomotion efficiency across animals and robots. It is defined as

$$CoT = \frac{P}{mgv}, \tag{3}$$

where P is the input power, m the system mass, g gravity, and v the forward velocity. Lower CoT values indicate more efficient locomotion. For animals, P represents metabolic power consumption, while for robots it represents the measured electrical input above idle baseline.

The LW SeaViper prototype reached the record speed of 33.2 cm/s (1.38 bl/s) while consuming 1.27 W, corresponding to a CoT of 6.1. However, the record CoT was achieved by the LN SeaViper prototype at a slower peak speed of 27.3 cm/s (1.13 bl/s) while consuming 548 mW. This corresponds to a minimum CoT of 3.9, improving upon [11]'s ground-based prototype's CoT of 46 by more than an order of magnitude. Although promising, this remains roughly one order of magnitude above the efficiency of aquatic animals of comparable mass. The velocity and CoT performance are plotted versus mass for a variety of aquatic animals [9], surface swimmers, tethered and untethered soft robots [19]–[30], and the ground prototype in Fig. 14-15

D. Electromechanical Conversion Efficiency

To better quantify the gap to biological performance and identify future design opportunities, we estimated the end-to-end electromechanical efficiency of the system. Under the best LN operating condition, the current sense amplifier recorded an additional 67 mA of average current drawn from the battery. At 8.2 V, this corresponds to an input electrical power of 548 mW. The two active piezoelectric actuators, each with a capacitance of 159 nF, therefore received an effective net stored power of $P = 2 \cdot \frac{1}{2} C V^2 f = 286$ mW. Based on the actuator coupling coefficient $k_{31}^2 \approx 0.15$, at most 15% of this electrical energy can be converted into mechanical work [13]. This sets an upper bound of 43 mW of mechanical power. In reality, this is an overestimate, as practical factors such as imperfect bonding between the actuator and steel substrate, non-ideal clamping, and adhesive losses further reduce this efficiency.

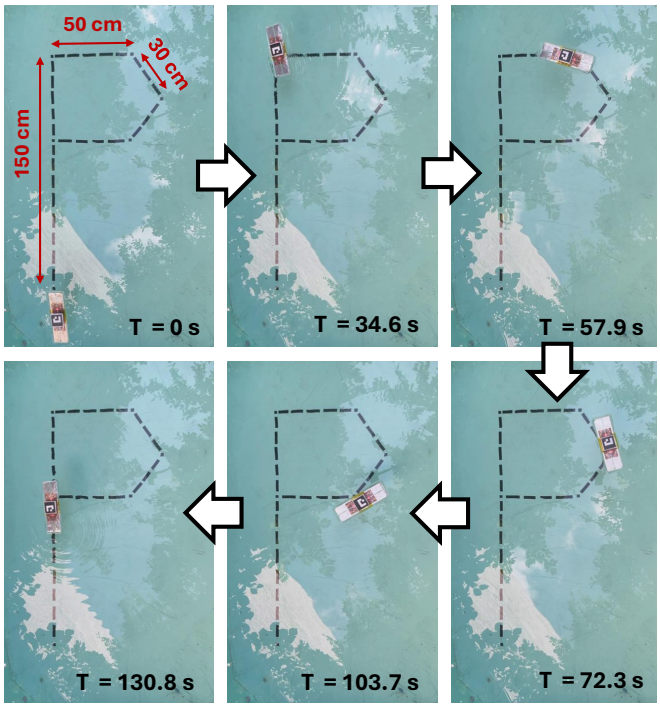

Fig. 16. Demonstration of autonomous feedback control of the LW SeaViper. The robot follows a "P"-shaped path approximately 310 cm long (≈13 body lengths). Each image depicts the arrival of SeaViper at a target.

From the measured robot performance ($v = 27.3$ cm/s, $F = 23$ mN), the useful mechanical output is only 6.3 mW. This yields an overall system efficiency from electrical power to "useful" mechanical power of 1.1%. The large disparity reflects intermediate losses in (i) power conversion, (ii) the intrinsic limiting ratio of electrical to mechanical power conversion in the piezoelectric actuators, and (iii) the fraction of mechanical power effectively directed into forward thrust. Addressing these losses would directly reduce power consumption, lowering CoT and extending runtime. In particular, efficiency could be significantly improved by recycling charge in the piezoelectric actuator instead of dissipating it to ground [31], [32]. Finally, future experiments that directly quantify fluid momentum transfer, such as particle image velocimetry, will provide further insight into how actuator work couples into useful thrust. While the actuator coupling coefficient (k_{31}) sets a 15% theoretical efficiency ceiling, there remains substantial room for improvement, and smart design choices informed by these experiments can move SeaViper closer to this limit.

E. Autonomous Feedback Control and Path Tracking

Real-time tiered feedback control was implemented using an ArUco marker and the Python OpenCV library. A three-state controller ("rotate–translate–arrive") used alignment, displacement, and their derivatives to select the appropriate mode. The prototype was capable of bidirectional translation at three speed tiers and rotation at two tiers. Waypoints defining the "P" path were derived from the overhead camera feed and referenced to the tape markers on the pool bottom. Because the aquatic robot experiences low drag and continues to drift when thrust ceases, the controller monitored angular and translational velocity as well as displacement error, applying approach-speed gating to minimize overshoot. Commands were sent at 10 Hz via serial link to the onboard ESP32. To reduce overshoot and ensure stable tracking, the robot was not operated at its maximum potential speed. The performance illustrated in Fig. 16 demonstrates SeaViper's ability to perform precise path tracking and engage with an environment on scales greater than its body length. Further development of this control will enable the use of its faster speeds and incorporate braking to maintain stability and precise stopping at each waypoint.

V. Conclusion

This work introduced SeaViper, a novel surface-swimming robot built upon our eViper topology developed in [10]–[12]. Three actuator–substrate configurations were fabricated and tested to investigate the influence of geometry and mass on resonance and locomotion. Prototype frequency response aligned well with preliminary theoretical cantilever beam analysis. The fastest prototype achieved a velocity of 33.2 cm/s (1.38 BL/s) and the most efficient achieved a cost of transport of 3.9, more than an order-of-magnitude improvement over prior ground-based prototypes. In addition, a real-time vision-based feedback controller enabled SeaViper to autonomously follow paths far exceeding its body length. This places SeaViper's surface performance in line with the forefront of its untethered submerged aquatic peers, clearly demonstrating the potential for this platform. A simple spring apparatus enabled measurement of thrust generation, and an efficiency analysis identified key loss mechanisms for future improvement. These results capture SeaViper's potential as a unique platform for the investigation of two-dimensional aquatic robots, enabling studies that can inform both bio-inspired design and future robotic applications.

References

[1] C. Laschi, B. Mazzolai, and M. Cianchetti, "Soft robotics: Technologies and systems pushing the boundaries of robot abilities," *Science Robotics*, vol. 1, no. 1, p. eaah3690, 2016. [Online]. Available: https://www.science.org/doi/abs/10.1126/scirobotics.aah3690

[2] D. Rus and M. T. Tolley, "Design, fabrication and control of soft robots," *Nature*, vol. 521, no. 7553, pp. 467–475, May 2015. [Online]. Available: https://doi.org/10.1038/nature14543

[3] M. Kulkarni, S. Edward, T. Golecki, B. Kaehr, and H. Golecki, "Soft robots built for extreme environments," *Soft Science*, vol. 5, no. 1, 2025. [Online]. Available: https://www.oaepublish.com/articles/ss.2023.51

[4] S. M. Youssef, M. Soliman, M. A. Saleh, M. A. Mousa, M. Elsamanty, and A. G. Radwan, "Underwater soft robotics: A review of bioinspiration in design, actuation, modeling, and control," *Micromachines*, vol. 13, no. 1, p. 110, 2022. [Online]. Available: https://doi.org/10.3390/mi13010110

[5] J. Qu, Y. Xu, Z. Li, Z. Yu, B. Mao, Y. Wang, Z. Wang, Q. Fan, X. Qian, M. Zhang, M. Xu, B. Liang, H. Liu, X. Wang, X. Wang, and T. Li, "Recent advances on underwater soft robots," *Advanced Intelligent Systems*, vol. 6, no. 2, p. 2300299, 2024. [Online]. Available: https://advanced.onlinelibrary.wiley.com/doi/abs/10.1002/aisy.202300299

[6] Y. Wang, H. Chen, J. Law, X. Du, and J. Yu, "Ultrafast miniature robotic swimmers with upstream motility," *Cyborg and Bionic Systems*, vol. 4, p. Article 0015, 2023. [Online]. Available: https://doi.org/10.34133/cbsystems.0015

[7] R. K. Katzschmann, J. DelPreto, R. MacCurdy, and D. Rus, "Exploration of underwater life with an acoustically controlled soft robotic fish," *Science Robotics*, vol. 3, no. 16, p. eaar3449, 2018. [Online]. Available: https://www.science.org/doi/abs/10.1126/scirobotics.aar3449

[8] H. Qing, J. Guo, Y. Zhu, Y. Chi, Y. Hong, D. Quinn, H. Dong, and J. Yin, "Spontaneous snapping-induced jet flows for fast, maneuverable surface and underwater soft flapping swimmer," *Science Advances*, vol. 10, no. 49, p. eadq4222, 2024. [Online]. Available: https://www.science.org/doi/abs/10.1126/sciadv.adq4222

[9] R. Baines, S. K. Patiballa, J. Booth, L. Ramirez, T. Sipple, A. Garcia, F. Fish, and R. Kramer-Bottiglio, "Multi-environment robotic transitions through adaptive morphogenesis," *Nature*, vol. 610, no. 7931, pp. 283–289, Oct 2022. [Online]. Available: https://doi.org/10.1038/s41586-022-05188-w

[10] N. Verma, Y. Hu, L. Huang, W. S. A. Rieutort-Louis, J. S. Robinson, T. Moy, B. Glisic, S. Wagner, and J. C. Sturm, "Enabling scalable hybrid systems: Architectures for exploiting large-area electronics in applications," *Proc. of the IEEE*, vol. 103, no. 4, pp. 690–712, 2015.

[11] H. Cheng, E. Veilleux, Z. Zheng, S. Wagner, N. Verma, J. C. Sturm, and M. Chen, "eviper-2d: A thin large-area soft robotics platform," in *2025 IEEE International Conference on Robotics and Automation (ICRA)*, May 2025, pp. 15 336–15 342.

[12] H. Cheng, Z. Zheng, P. Kumar, Y. Chen, J. Baek, B. Kim, S. Wagner, N. Verma, J. C. Sturm, and M. Chen, "A flexible lightweight 7.4 v input 300 v to 1500 v output power converter for an untethered modular piezoelectric soft robot," in *IEEE 24th Workshop on Control and Modeling for Power Electronics (COMPEL)*, 2023, pp. 1–7.

[13] "Smart Material Corp. Sarasota, Florida. Part numbers: M-5628-P2, M-8514-P2, M-8528-P2." [Online]. Available: https://www.smart-material.com/media/Datasheets/MFC_V2.4-datasheet-web.pdf

[14] K. Iguchi, T. Shimooka, S. Uchikai, Y. Konno, H. Tanaka, Y. Ikemoto, and J. Shintake, "Agile robotic fish based on direct drive of continuum body," *npj Robotics*, vol. 2, no. 1, p. 7, 2024. [Online]. Available: https://doi.org/10.1038/s44182-024-00014-z

[15] C. A. Van Eysden and J. E. Sader, "Resonant frequencies of a rectangular cantilever beam immersed in a fluid," *Journal of Applied Physics*, vol. 100, no. 11, p. 114916, 12 2006. [Online]. Available: https://doi.org/10.1063/1.2401053

[16] D. Sedlar, Z. Lozina, and D. Vučina, "Experimental investigation of the added mass of the cantilever beam partially submerged in water [eksperimentalno istraživanje dodane mase na gredi djelomično uronjenoj u vodu]," *Tehnicki Vjesnik*, vol. 18, pp. 589–594, 12 2011.

[17] J. N. Newman, *Marine Hydrodynamics*. Cambridge, MA: MIT Press, 1977.

[18] J. Videler and B. Nolet, "Costs of swimming measured at optimum speed: Scale effects, differences between swimming styles, taxonomic groups and submerged and surface swimming," *Comparative Biochemistry and Physiology Part A: Physiology*, vol. 97, no. 2, pp. 91–99, 1990. [Online]. Available: https://www.sciencedirect.com/science/article/pii/030096299090155L

[19] T. Li, G. Li, Y. Liang, T. Cheng, J. Dai, X. Yang, B. Liu, Z. Zeng, Z. Huang, Y. Luo, T. Xie, and W. Yang, "Fast-moving soft electronic fish," *Science Advances*, vol. 3, no. 4, p. e1602045, 2017. [Online]. Available: https://www.science.org/doi/abs/10.1126/sciadv.1602045

[20] Y. Chi, Y. Hong, Y. Zhao, Y. Li, and J. Yin, "Snapping for high-speed and high-efficient butterfly stroke–like soft swimmer," *Science Advances*, vol. 8, no. 46, p. eadd3788, 2022. [Online]. Available: https://www.science.org/doi/abs/10.1126/sciadv.add3788

[21] J. Zhu, C. White, D. K. Wainwright, V. D. Santo, G. V. Lauder, and H. Bart-Smith, "Tuna robotics: A high-frequency experimental platform exploring the performance space of swimming fishes," *Science Robotics*, vol. 4, no. 34, p. eaax4615, 2019. [Online]. Available: https://www.science.org/doi/abs/10.1126/scirobotics.aax4615

[22] T. Bujard, F. Giorgio-Serchi, and G. D. Weymouth, "A resonant squid-inspired robot unlocks biological propulsive efficiency," *Science Robotics*, vol. 6, no. 50, p. eabd2971, 2021. [Online]. Available: https://www.science.org/doi/abs/10.1126/scirobotics.abd2971

[23] J. Shintake, V. Cacucciolo, H. Shea, and D. Floreano, "Soft biomimetic fish robot made of dielectric elastomer actuators," *Soft Robotics*, vol. 5, no. 4, pp. 466–474, 2018, pMID: 29957131. [Online]. Available: https://doi.org/10.1089/soro.2017.0062

[24] Y. Tang, Y. Chi, J. Sun, T.-H. Huang, O. H. Maghsoudi, A. Spence, J. Zhao, H. Su, and J. Yin, "Leveraging elastic instabilities for amplified performance: Spine-inspired high-speed and high-force soft robots," *Science Advances*, vol. 6, no. 19, p. eaaz6912, 2020. [Online]. Available: https://www.science.org/doi/abs/10.1126/sciadv.aaz6912

[25] H. Qing, J. Guo, Y. Zhu, Y. Chi, Y. Hong, D. Quinn, H. Dong, and J. Yin, "Spontaneous snapping-induced jet flows for fast, maneuverable surface and underwater soft flapping swimmer," *Science Advances*, vol. 10, no. 49, p. eadq4222, 2024. [Online]. Available: https://www.science.org/doi/abs/10.1126/sciadv.adq4222

[26] S.-J. Park, M. Gazzola, K. S. Park, S. Park, V. Di Santo, E. L. Blevins, J. U. Lind, P. H. Campbell, S. Dauth, A. K. Capulli, F. S. Pasqualini, S. Ahn, A. Cho, H. Yuan, B. M. Maoz, R. Vijaykumar, J.-W. Choi, K. Deisseroth, G. V. Lauder, L. Mahadevan, and K. K. Parker, "Phototactic guidance of a tissue-engineered soft-robotic ray," *Science*, vol. 353, no. 6295, pp. 158–162, 2016. [Online]. Available: https://doi.org/10.1126/science.aaf4292

[27] K. Y. Lee, S.-J. Park, D. G. Matthews, S. L. Kim, C. A. Marquez, J. F. Zimmerman, H. A. M. Ardoña, A. G. Kleber, G. V. Lauder, and K. K. Parker, "An autonomously swimming biohybrid fish designed with human cardiac biophysics," *Science*, vol. 375, no. 6581, pp. 639–647, 2022. [Online]. Available: https://doi.org/10.1126/science.abh0474

[28] R. K. Katzschmann, J. DelPreto, R. MacCurdy, and D. Rus, "Exploration of underwater life with an acoustically controlled soft robotic fish," *Science Robotics*, vol. 3, no. 16, p. eaar3449, 2018. [Online]. Available: https://www.science.org/doi/abs/10.1126/scirobotics.aar3449

[29] J. Ko, C. Kim, D. Kim, Y. Song, S. Lee, B. Yeom, J. Huh, S. Han, D. Kang, J.-S. Koh, and J. Cho, "High-performance electrified hydrogel actuators based on wrinkled nanomembrane electrodes for untethered insect-scale soft aquabots," *Science Robotics*, vol. 7, no. 71, p. eabo6463, 2022. [Online]. Available: https://www.science.org/doi/abs/10.1126/scirobotics.abo6463

[30] F. Berlinger, M. Saadat, H. Haj-Hariri, G. V. Lauder, and R. Nagpal, "Fish-like three-dimensional swimming with an autonomous, multi-fin, and biomimetic robot," *Bioinspiration & Biomimetics*, vol. 16, no. 2, p. 026018, feb 2021. [Online]. Available: https://dx.doi.org/10.1088/1748-3190/abd013

[31] D. Campolo, M. Sitti, and R. S. Fearing, "Efficient charge recovery method for driving piezoelectric actuators with quasi-square waves," *IEEE Transactions on Ultrasonics, Ferroelectrics, and Frequency Control*, vol. 50, no. 3, pp. 237–244, Mar 2003.

[32] T. Ozaki and N. Ohta, "Power-efficient driver circuit for piezo electric actuator with passive charge recovery," *Energies*, vol. 13, no. 11, 2020. [Online]. Available: https://www.mdpi.com/1996-1073/13/11/2866